Oil & Natural Gas Technology

DOE Award No.: DE-FC26-06NT43067

Quarterly Progress Report (July – September 2011)

Mechanisms Leading to Co-Existence of Gas and Hydrate in Ocean Sediments

Submitted by:
Massachusetts Institute of Technology
77 Massachusetts Ave
Cambridge, MA 02139

The University of Texas at Austin
1 University Station C0300
Austin, TX 78712-0228

Prepared for:
United States Department of Energy
National Energy Technology Laboratory

October 30, 2011

Office of Fossil Energy

Executive summary

Work during this period of performance has focused on research activities under Task 8 (Modeling methane transport at the bed scale).

In this report, we describe the development of a simple, mechanistic model of methane migration with hydrate formation and dissociation through soft sediments, building on previous work of methane venting [35]. It is well documented that free gas can traverse the hydrate stability zone, often through preferential pathways, such as fractures and faults. We hypothesize that the observed episodicity of bubble venting (ebullition) into the water column is controlled by the dilation of dynamic flow paths in response to changes in effective stress, both from fluid pressurization associated with the methane source and from tidal loading on the sediment surface. In previous work, we have captured the temporal distribution of methane venting from lake sediments using a 1D continuum numerical model of gas release through such "breathing" dynamic flow conduits that respond to a hydrostatic forcing. Here, we model a characteristic shallow, hydrate-bearing region in order to explore how fracture flow, tidal forcing and hydrate formation interact to determine the episodicity and magnitude of methane released into the water column. We identify two time scales that interact with the tidal period to determine the episodicity of release, and we find that the amount of gas released to the ocean depends critically on the vertical gas conductivity and kinetic hydrate formation rate.

Technology transfer activities

During this reporting period, 5 papers were written and the corresponding presentations were given at the 2011 International Conference on Gas Hydrates, which took place in Edinburgh, UK.

Two other papers were published in *Geophysical Research Letters*, one on the thermodynamic and hydrodynamic controls on the overpressure caused by hydrate dissociation [17], and one on the experimental verification, at reservoir conditions, of the crossover from fingering to fracturing [8].

Discussion of activities in this reporting period

Task 8: Modeling methane transport at the bed scale

NUMERICAL MODELING OF HYDRATE FORMATION AND METHANE GAS TRANSPORT THROUGH DYNAMIC CONDUITS

Abstract. Methane is a potent greenhouse gas that is generated geothermally and biologically in lake and ocean sediments. The mode of methane transport impacts the distribution of hydrates in the sediment, as well as the magnitude of releases into the water column and atmosphere. It is well documented that free gas can traverse the hydrate stability zone, often through preferential pathways, such as fractures and faults. We hypothesize that the observed episodicity of bubble venting (ebullition) into the water column is controlled by the dilation of dynamic flow paths in response to changes in effective stress, both from fluid pressurization associated with the methane source and from tidal loading on the sediment surface. In previous work, we have captured the temporal distribution of methane venting from lake sediments using a 1D continuum numerical model of gas release through such "breathing" dynamic flow conduits that respond to a hydrostatic forcing. Here, we model a characteristic shallow, hydrate-bearing region in order to explore how fracture flow, tidal forcing and hydrate formation interact to determine the episodicity and magnitude of methane released into the water column. We identify two time scales that interact with the tidal period to determine the episodicity of release, and we find that the amount of gas released to the ocean depends critically on the vertical gas conductivity and kinetic hydrate formation rate.

Introduction. The dissociation of methane hydrates in shallow ocean sediments has long been suggested as a potential feedback to climate change [2, 3, 11, 19, 20]. One of the primary modes of methane export from submerged sediments is free-gas ebullition, but gas bubbles dissolve during rise, exposing the methane to oxidation to the less potent greenhouse gas CO_2 [44]. The ability of rising bubbles to transport methane to the atmosphere depends on the release depth, bubble density and size distribution [15, 16, 25, 26, 29]. Thus, the atmospheric release depends not only on how much hydrate dissociates but how it is released from the sediments.

Focused ebullition has been observed at Hydrate Ridge, especially in a periodic pattern during low tides [40, 41]. The gas is likely supplied from a deep geologic reservoir, but the mechanism that allows it to travel through the Hydrate Stability Zone (HSZ) from near the base of the HSZ (BHSZ) and to escape only during low tides has yet to be determined. Multiple mechanisms have been proposed for coexistence of free gas & hydrates in the HSZ [30, 34, 42]: (1) regional geotherms, (2) reduction in hydrate stability by salt accumulation, (3) kinetics of hydrate formation, and (4) fast, focused flow of free gas through high-permeability conduits. Evidence of fractures and flow through them at Hydrate Ridge has been inferred from field observations [13, 41, 43, 47] and modeling studies [10, 28].

The combined observations of tidally-controlled ebullition with evidence of gas flow through conduits gives us an opportunity to investigate the mechanisms controlling gas migration through the hydrate stability zone. Previous modeling work has sought to esti-

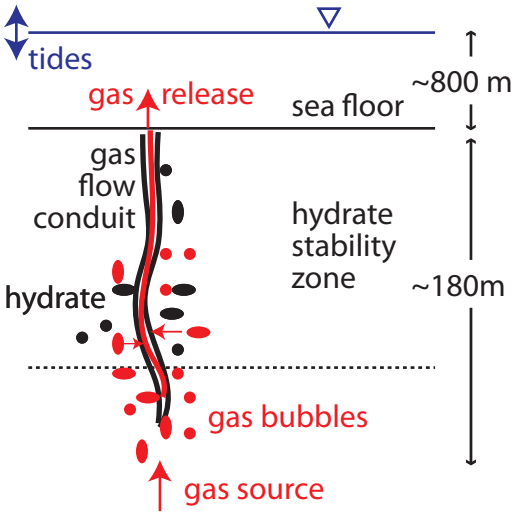

Figure 1: Conceptual model of gas flowing through the hydrate stability zone by dilating near-vertical conduits. These conduits access gas in a small domain of surrounding porous media, especially through conductive horizontal strata [47], and transport the gas vertically. Vertical dimensions reflect the south summit of Hydrate Ridge, where tidally-forced ebullition has been observed [40, 41].

mate the distribution of hydrates by considering methane transport in the dissolved phase only [7, 10, 48] or as gas flowing by capillary invasion [9, 14, 28, 33]. These models capture slow processes of pore water flow, heat and salt transport to capture important impacts on hydrate stability and the equilibrium distribution of hydrates [23]. Other models have been used to estimate the hydrate response to slow sea level change [27] and the onset time for fracturing [9, 10, 28].

In contrast, we model fast processes of free-gas flow through fractures, tidal variations, and kinetic hydrate formation. Previous modeling of gas release from hydrate-free lake sediments has shown that conduit flow can reproduce the observed, hydrostatically-forced episodicity of gas venting [36], and we hypothesize that a similar mechanism controls tidally-forced venting from hydrate-bearing sediments. Here, we develop a numerical model of this mechanism and show that it can indeed reproduce the tidally-dependent ebullition record observed at Hydrate Ridge. In addition, we find that within a tidal low the ebullition will manifest as distinct bursts that arise from a geyser-like instability. The ability of gas to traverse the HSZ depends on the vertical gas conductivity and kinetic hydrate formation rate.

Theory, formulation, and methods.

Model domain. We investigate the dynamics of gas flow through the hydrate stability zone with a one-dimensional, continuum-scale numerical model. The model attempts to capture the aggregate behavior of sediments fractured periodically in space. Because the model is 1D, the transport and accumulation reflect the vertical flow through the fractures

as well as the fluid exchange between the fracture and the sediment matrix.

The model is intended to resolve the release of methane at sub-tidal timescales (minutes to hours). At this timescale, fast transport mechanisms such as gas-phase flow are expected to dominate pore-fluid solute advection and diffusion. Thus, we neglect the accumulation and transport of dissolved methane, salt, and heat, with hydrate formation and aqueous flow. These mechanisms control the hydrate distribution by changing the local hydrate stability conditions [4, 10, 14, 27, 28] and thus the long-term hydrate distribution. In turn, hydrate formation can influence the transport regime by cementing the grains [22, 45] or clogging the pores [10, 28, 32]. We neglect these slow feedback mechanism to develop a simple continuum model of fast gas flow through conduits that respond to both internal pressurization and a tidal forcing.

Poromechanics. Gas behaves differently in fine-grained sediments, such as the clay-dominated sediments found in the HSZ at Hydrate Ridge [43], compared with coarse-grained sediments. Gas invades large-grained porous media when the capillary pressure ($P_g - P_w$) becomes large enough for the curved interface to squeeze through a pore throat. In fine-grained sediments, gas invades by deforming the grains because the capillary pressure required to squeeze through the throats is prohibitively large [18]. Instead of small interstitial bubbles characteristic of a capillary-controlled system, gas bubbles in fine sediments take the form relatively large gas cavities surrounded by a matrix of water and sediment grains [37]. Because these bubbles grow in a highly-eccentric, cornflake-shaped fracture pattern [1, 6], rather than as spherical bubbles, this mode of growth may also allow for vertical mobility.

The effective stress, σ', controlling the deformation of this continuum around the gas cavities may then be approximated as,

$$\sigma' = \sigma_h - P_g, \tag{1}$$

where σ_h is the horizontal stress and P_g is the gas pressure [36]. This contrasts with the typical form of the effective stress, in which the fluid pressure of concern is the water pressure [10, 38] or when both fluid pressures are considered [5, 22]. Equation 1 is consistent with the view that sediment and water form a coherent "mud" phase against which large gas bubbles must push to expand.

The deformation of this matrix-water continuum may be treated as a plastic process that occurs at yield limits in tension (σ_T) and compression (σ_C):

$$-\sigma_T \leq \sigma' \leq \sigma_C. \tag{2}$$

Cavities dilate in tension ($\sigma' = -\sigma_T$), reducing the gas pressure sufficiently to maintain the plastic equilibrium defined in Equation 2. In compression ($\sigma' = \sigma_C$), the cavities shrink and the gas pressure rises in step with the horizontal stress. This mechanism of cavity deformation is used to attribute accumulation of gas mass to changes in pressure and volume, in the following order as necessary:

1. Generate maximum gas pressure change at current volume, up to a plastic yield limit

$$\Delta P_g^{max} = \frac{\Delta M_g RT}{S_g \phi m_{CH_4}}. \tag{3}$$

2. If a yield limit is reached, deform cavities to change volume. Vary saturation at the new fixed gas pressure, according to the ideal gas law, up to a maximum that satisfies the volume constraints $S_g + S_h \leq 1$ and $S_g \geq S_g^{min}$.

3. If a volume constraint is reached, allow pressure to rise or fall outside the plastic limits ($\sigma_h - \sigma_C \leq P_g \leq \sigma_h + \sigma_T$) at the new fixed saturation according to the ideal gas law.

Thus, gas accumulation first forces the gas pressure to a yield limit before changing the gas saturation. This allows for compressible gas flow but requires a small time step to resolve frequent pressure changes.

In all simulations here we assume $\sigma_C = 0$ and $\sigma_T = 0.3$ MPa, consistent with estimates from combined modeling and field observations at South Hydrate Ridge [47]. The gas pressure may exceed the plastic yield limits, especially when hydrate formation depletes the gas to a minimum saturation (for stability) $S_g^{min} = 0.005$. However, this does not occur in any of the simulations shown here.

Gas flow through conduits. The core of our model is free-gas flow through dynamic, vertical conduits. These conduits dilate at the tensile plastic yield limit and close at the compressive limit (Figure 2). In addition to the dependence on effective stress, we impose a minimum gas saturation, $S_g^{conduit} = 0.1$, which is required for the conduits to connect across depth intervals [47]. Similar model behavior is obtained when $S_g^{conduit} = 0$, except the low gas saturations exacerbate the gas pressure fluctuations during cavity deformation (Equation 3), and resolving these larger pressure swings requires a smaller time step.

The model captures gas flow through fractured porous media without distinguishing the pools of gas in the conduit and porous medium separately. Instead, the effect of dilation is captured by increasing the vertical intrinsic permeability, k, from 0 to a parameterized permeability of the conduit-matrix continuum, $k_{conduit}$, which accounts for both the dimensions and lateral spacing of conduits. The gas mass conservation equation uses a multiphase extended form of Darcy's law for the gas flux [31]:

$$\frac{\partial(\phi \rho_g S_g)}{\partial t} = -\frac{\partial F_g}{\partial z} + Q_g^h \tag{4}$$

$$F_g = -\rho_g \frac{k k_{rg}}{\mu_g} \left(\frac{\partial P_g}{\partial z} - \rho_g g \right) \tag{5}$$

$$k_{rg} = S_g \tag{6}$$

where Q_g^h is the rate of gas mass generation from hydrate per unit volume and constitutes all the gas loss from hydrate dissociation, Q_h:

$$Q_g^h = -\chi_h^{CH_4} Q_h \tag{7}$$

The model is initially free of hydrate but includes gas saturations equal to the minimum for conduit opening, $S_g^{conduit}$, in order to eliminate the initial time necessary to accumulate this minimum saturation. The gas pressure, however, is assumed to begin at the compressive yield limit so that the conduit is initially closed everywhere. At the top boundary the gas pressure equals the tidally-forced hydrostatic pressure, with $S_g = 0$, and the gas flux in the bottom is set by the parameter F_g^{source}, which represents the source supplied through Horizon A at the BHSZ [43, 47].

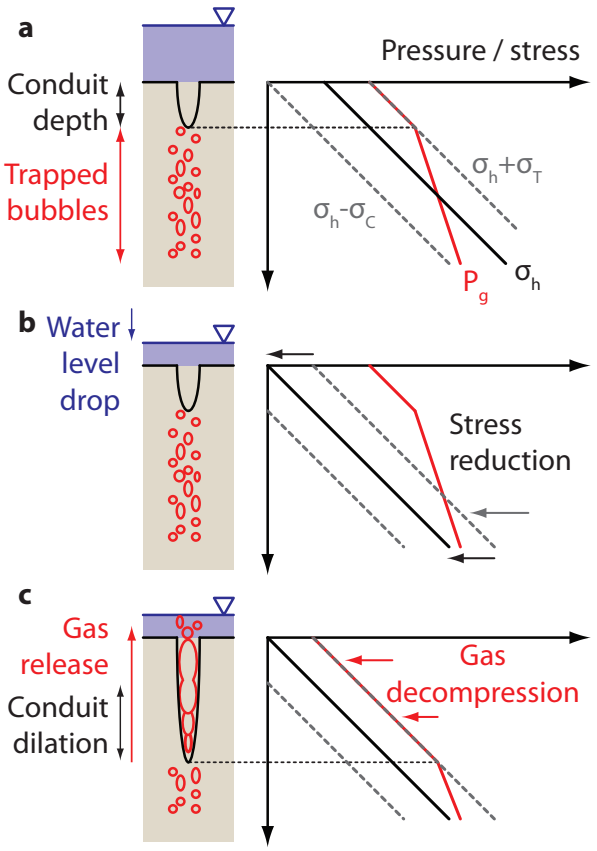

Figure 2: Model response to water level drop. (a) Initial condition: the cartoon at left shows the water level (blue) above a sediment column with gas bubbles trapped below the open conduit (not to scale in vertical). The conduit opens when the effective stress, $\sigma' = \sigma_h - P_g$, falls to its tensile yield limit, $-\sigma_T$. The stress and pressure profiles at right show that this occurs when P_g (red solid line) equals $\sigma_h + \sigma_T$ (gray dashed line). (b) A drop in hydrostatic load reduces σ_h throughout the sediment column. (c) Plastic cavity dilation allows shallow gas bubbles to decompress to $\sigma + \sigma_T$. The conduit opens from the deepest location where $\sigma' = -\sigma_T$ and releases the formerly trapped bubbles. In the case of a hydrostatic load increase (not shown), the stress rises, and the cavity compression mechanism pressurizes gas bubbles to enforce $\sigma' \leq \sigma_C$, or equivalently $P_g \geq \sigma_h - \sigma_C$. On open conduit remains open until this compressive limit is reached. Modified from [36].

Hydrate formation and dissociation. Given the high temporal resolution of the model (seconds to minutes), a kinetic model of hydrate formation was adopted following [21]. The model for microscale hydrate formation is driven by the departure from equilibrium fugacity, and we simplify this by considering the nearly-equivalent departure from equilibrium pressure [12]. We also adopt the same temperature dependence but neglect the dependence on surface area of hydrate [21]. The rate of hydrate mass generation per bulk volume is:

$$Q_h = K_h(P_g - P_{eq}) \exp(-\frac{E}{RT}), \tag{8}$$

where K_h is a rate constant with units of kg/m^3/Pa/s, $E = 8.1 \times 10^4$ J/mol is the activation energy of the reaction, $R = 8.314$ J/mol/K is the gas constant. This model transfers mass of CH_4 from the gas to hydrate phases when $P_g > P_{eq}$, in the hydrate stability zone, and it transfers mass in the other direction when $P_g < P_{eq}$, generally below the hydrate stability zone. The equilibrium pressure is evaluated as the hydrate-gas phase boundary, $P_{eq}[\text{kPa}] = \exp(40.234 - 8860/T[\text{K}])$ [24], for a temperature profile from a seafloor temperature of 277 K and constant geothermal gradient of 0.053 K/m at Hydrate Ridge [10]. This causes hydrate to form slightly below the traditional BHSZ, defined as $P_w = P_{eq}$, because $P_g \geq P_w$ when free gas is present. Whenever either phase is depleted or when the sum of gas and hydrate saturations exceeds 1, the rate of transfer is reduced to avoid unphysical mass transfer.

Tidal forcing. A central goal of our model is to capture the observed relationship between tides and ebullition from hydrate-bearing sediments [41], and the link is made through the impact of hydrostatic pressure on total and effective stresses. The total vertical (lithostatic) stress, σ_v, is the sum of the hydrostatic pressure at the sea floor and the integrated bulk density:

$$\sigma_v(z,t) = P_h(t) + \int_0^z \rho_b(z')g dz' \tag{9}$$

$$P_h(t) = \rho_w g \left(D + z_{tide} * \sin\left(\frac{2\pi t}{t_{tide}}\right)\right), \tag{10}$$

where ρ_b is the bulk density, P_h is the hydrostatic pressure at the seafloor, z_{tide} and t_{tide} are the tidal amplitude and period, respectively. These equations simply show that tidal variations reflect the total vertical stress throughout the HSZ.

The total vertical stress varies with tides as shown above, but near-vertical conduits should in the direction where the gas opposes the minimum stress, which is generally horizontal near the crest of south Hydrate Ridge [47]. We calculate the horizontal stress that would be imposed on the model domain by the surrounding, water-saturated sediments. The vertical and lateral stresses are connected through the water-saturated effective stresses by the lateral stress coefficient, K_0. In water-saturated rock and soil, K_0 may be expressed as

$$K_0 = \frac{\sigma'_{hw}}{\sigma'_{vw}} = \frac{\nu}{1-\nu}, \tag{11}$$

where $\sigma'_{hw} = \sigma_h - P_w$ and $\sigma'_{vw} = \sigma_v - P_w$ are the water-saturated effective stresses, and ν is Poisson's ratio [46]. We adopt $\nu = 3/7 \rightarrow K_0 = 0.75$ and for our system [39]. Estimating

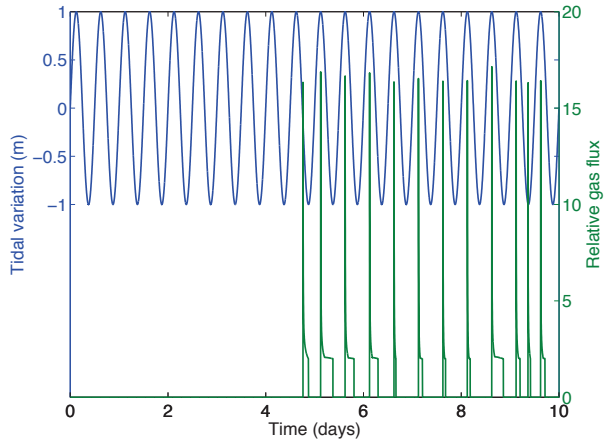

Figure 3: Periodic venting of gas (green, right scale) at the seafloor in response to 1 m tidal signal (blue, left scale). Gas flux is normalized by the input flux at the bottom of the model, F_g^{source}. The delay before the initial release reflects the timescale for gas to build up pressure and traverse the HSZ. The strong peak leading each release reflects a buildup of pressure just below the seafloor that is released during plastic tensile opening of the gas flow conduit at the surface, after which the gas pressure drive is reduced. Gas vents only during falling tides.

the horizontal stress from the vertical stress requires both the lateral stress coefficient and water pressure:

$$\sigma_h = \sigma'_{hw} + P_w = K_0\sigma_v + (1 - K_0)P_w \tag{12}$$

The water pressure response on short timescales and deep in sediments is undrained, where the fluid pressurization with laterally-uniform variations in vertical stress is determined by the loading efficiency, $\lambda = \partial P_w/\partial\sigma_v$ [46]. For the water-saturated sediments surrounding the model domain, we assume $\lambda = 1$ [27], and therefore that the water pressure changes synchronously and in the same amount as vertical stress.

Combined model. During each time step, the mechanisms are applied in a staggered manner:

1. Impose hydrostatic forcing.
2. Determine where conduits open and close to impose permeability profile.
3. Flow gas through the open conduits.
4. Exchange mass between gas and hydrate phases.
5. Deform cavities, altering P_g and S_g, to plastic equilibrium in response to the hydrostatic forcing and the mass accumulation combined from flow and phase transfer.

Results.

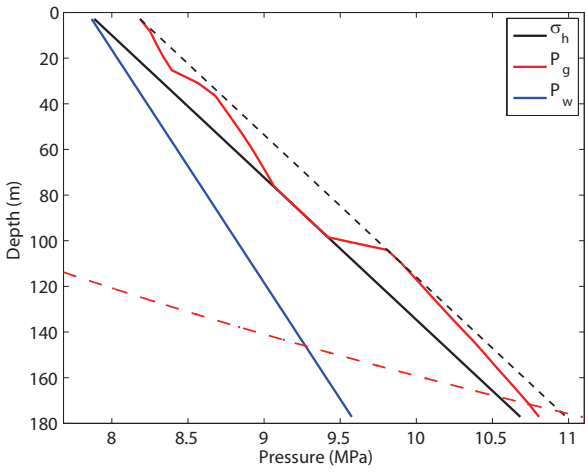

Figure 4: Profile of pressures and stresses at the end of the base simulation. The horizontal stress, gas and water pressures appear as solid lines of black, red and blue, respectively. The tensile limit on gas pressure, $\sigma_h + \sigma_T$, is shown as a dotted black line, and the equilibrium gas pressure, P_{eq} is a red dashed curve. The region from $0 - 80$ mbsf is a connected gas plume where the conduit remains open because $P_g > \sigma_h - \sigma_C$. This plume is separated from the other rising plume, from $100 - 180$ mbsf, by a region where the gas pressure has fallen to the compressive yield limit and the conduit has closed.

Episodicity of gas release at the seafloor. We perform a base-case scenario designed to reproduce the general pattern of ebullition during tidal lows for conditions observed at the southern summit of Hydrate Ridge [41]. The parameter values used for this base scenario are $D = 800$ m, $H = 180$ m, $z_{tide} = 1$ m, $t_{tide} = 12$ hours, $k_{conduit} = 2 \times 10^{-14}$ m^2, $K_h = 100$ kg/m^3/Pa/s, $F_g^{source} = 10^{-4}$ kg/m^2/s, $\sigma_T = 0.3 \times 10^6$ Pa, and $S_g^{conduit} = 0.1$. Under these conditions gas indeed traverses the HSZ and escapes during falling tides (Figure 3).

The time for gas to traverse the HSZ may be estimated using the multiphase Darcy flux (Equation 5):

$$t_{flow} \sim \frac{z_{BHSZ} \mu_g \phi}{k_{conduit} \rho_b g}, \tag{13}$$

where the characteristic gas pressure gradient has been approximated by a characteristic value relative to the lithostatic gradient, $\rho_b g$. The model predicts that gas typically accumulates beneath the sediment surface until the hydrostatic pressure falls with tides (Figure 4) and the tensile plastic deformation at the surface allows gas to escape into the water column. After an initial peak in gas flux, the ebullition continues at a moderate rate until the near-surface gas is depleted or the tides begin to rise again and cause the conduits to close (Figure 3).

Timescales of flow through dynamic conduits. Even without a tidal forcing or hydrate formation, compressible gas flow through a system of dynamic conduits displays two primary time scales at steady state: the release time for a connected gas plume, and the duration of an individual ebullition event. Each rising gas plume, displayed as a region of gas pressure elevated above the horizontal stress and the conduit remains open (Figure 4), may

reach the sediment surface and escape over a time period on the order of 1 day (Figure 5, top). This release time scales as

$$t_{plume} \sim t_{flow} \frac{h_{plume}}{z_{BHSZ}}, \tag{14}$$

where h_{plume} is the height of a rising gas plume. This height depends on the ratio of gas influx from below (F_g^{source}) and the vertical conductivity and may be estimated as

$$h_{plume} \sim t_{flow} \frac{F_g^{source}}{M_g^0}, \tag{15}$$

where M_g^0 is the initial mass of gas per unit bulk volume. This equation yields an estimate of ~ 130 m for the base simulation and agrees well with the observed heights of ~ 100 m in Figure 4.

However, a plume is not necessarily released in a continuous event. The release of methane gas from the top of the sediment column locally reduces the gas pressure and can close the conduit before the underlying gas plume is depleted. This geyser-like instability releases a rising gas plume as multiple separate ebullition events (Figure 5, bottom).

Interaction of flow with tides and hydrates. The inherent episodicity of gas release through conduits is complicated by the influence of tides and hydrate formation. The relatively slow release of a connected plume may be broken up into individual releases as falling tides facilitate conduit opening by reducing the hydrostatic load and total stress (Equation 9 and Figure 6, top). The release during a single cycle may then be further divided by the geyser instability (Figure 6, bottom).

Hydrate formation simultaneously reduces the gas pressure and closes the conduits more quickly, which delays the arrival at the surface, reduces the total output of gas, and changes the fine-scale episodicity of gas release (Figure 7).

Gas survival through the HSZ. The amount of methane that traverses the HSZ depends on the relative rates of gas flow and conversion to hydrate. The time required for gas to traverse the HSZ is estimated from Equation 13, although the flow timescale itself depends on the rate of hydrate formation because hydrate formation tends to close the conduits or prevent their opening by reducing the gas pressure. The flow timescale should be compared with the timescale for hydrate formation, which may be estimated from Equation 8 as the time required to consume the initial gas at its initial pressure:

$$t_{hydrate} \approx \frac{M_g^0 / \chi_{CH_4}^h}{K_h (P_g - P_{eq}) \exp(-E/(RT))}, \tag{16}$$

where $\chi_{CH_4}^h$ is the mass fraction of methane in hydrates. Because the initial pressure and temperature profiles are not spatially uniform, $t_{hydrate}$ is estimated as the average over all depth intervals.

We quantify the fraction of methane flowing through the model that reaches the ocean by tracking these fluxes over the course of a given simulation. If the time period is long

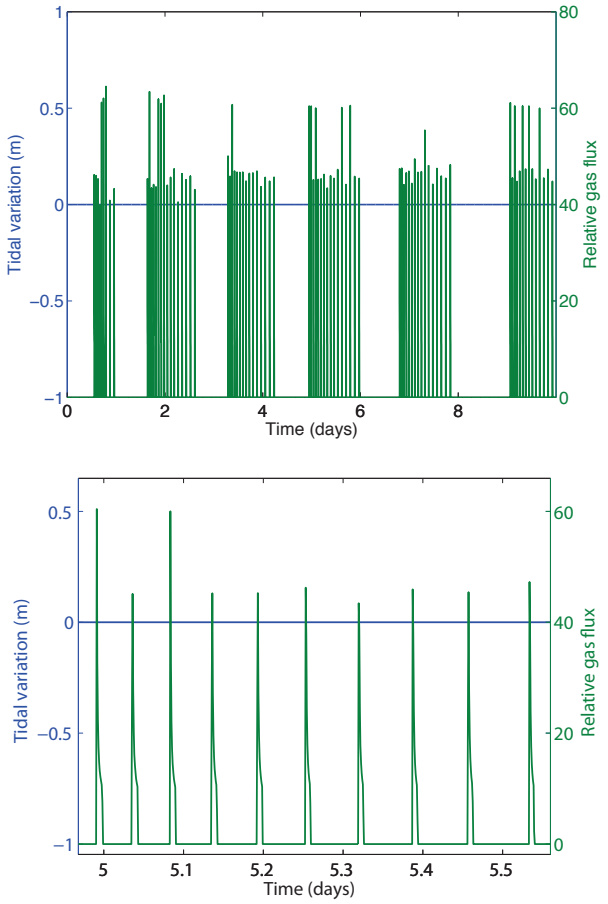

Figure 5: Time series showing an internally-driven run with no tidal forcing. The top figure shows two timescales relevant to the release: a longer timescale created by the rise of connected gas plumes, which vent for and are separated by about a day, and a shorter timescale of discrete ebullition events. The zoomed bottom figure shows that these releases are separated by about 1/20 day.

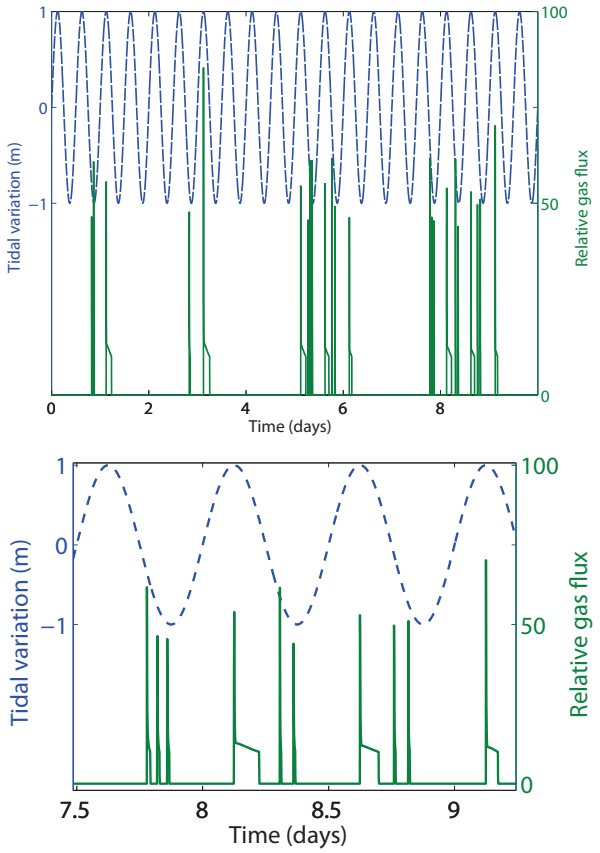

Figure 6: Impact of combined internal and external forcings on gas flow without hydrate formation. Top: time series showing the long timescale of plume release of $\sim$ 2 days (days 1,3, 5, and 8) along with other effects within each plume release. Bottom: zoom of the top figure shows that, within a given plume release, the individual ebullition events occur only during falling tides and display different geyser-driven episodicity depending on the pressure and saturation conditions in the near-surface sediments.

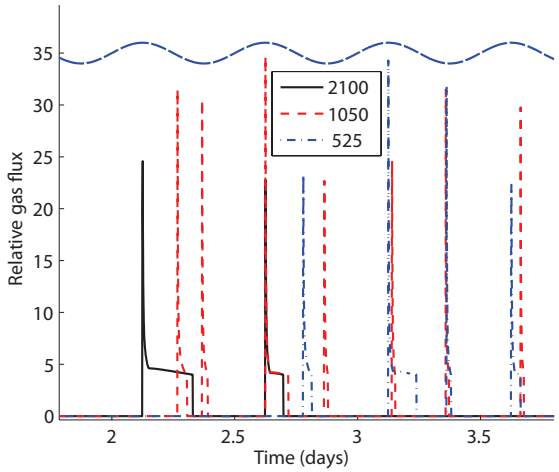

Figure 7: Sensitivity of venting timeseries to rate of hydrate formation. In all cases, $k_{conduit} = 5 \times 10^{-14}$ m^2, $z_{tide} = 1$ m (blue dashed sinusoid centered on 35 on the vertical axis), and K_h is varied to control the ratio $t_{hydrate}/t_{flow}$, shown in the legend. Smaller values of $t_{hydrate}/t_{flow}$ relate to faster hydrate conversion and both delay the first ebullition event and reduce the total gas vented to the ocean and (see Figure 8).

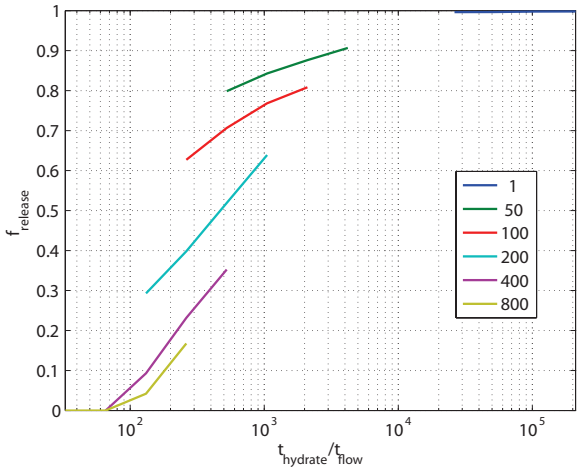

Figure 8: Sensitivity of gas release to rates of gas flow and hydrate formation. The fraction of gas that escapes without conversion to hydrate, $f_{release}$, increases as the timescale of hydrate formation increases relative to the timescale of flow. The timescale ratio $t_{hydrate}/t_{flow}$ was varied using both $k_{conduit}$ and K_h. The legend shows particular values of K_h, and the discontinuities show that the release fraction is somewhat dependent on $t_{hydrate}$ independently of $t_{hydrate}/t_{flow}$.

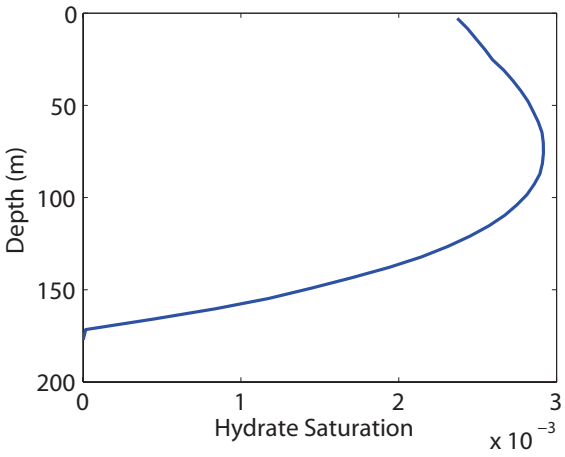

Figure 9: Final hydrate saturation profile for the same conditions as in Figure 3 after 10 days.

enough to reach pseudo-steady state conditions, changes in the methane storage become small relative to the cumulative fluxes into and out of the system. In this case, the ability of methane to escape to the sediment surface may be estimated as the ratio of time-integrated fluxes across the top and bottom of the model. However, the poorly-constrained initial gas content of the system motivates us to account for the change in *gas* storage over the time period:

$$\Delta M_g = \int_0^H \left(M_g(z, t_f) - M_g(z, t = 0) \right) dz \tag{17}$$

$$f_{release} \approx \frac{\int_0^{t_f} F(z = 0, t) dt}{\int_0^{t_f} F(z = H, t) dt - \Delta M_g}, \tag{18}$$

where $M_g = \rho_g S_g \phi$ is the mass of accumulated gas per volume. This release fraction is highly sensitive to the ratio of flow and hydrate timescales, and it also depends on the hydrate generation rate (Figure 8).

Vertical hydrate distribution. Hydrate formation increases the saturation of hydrate, but the assumed formation rates are slow and cause little to appear during the course of simulations here. A profile of hydrate saturation shows this growth throughout the HSZ (Figure 9). The distribution reflects the balance of the driving force, $P_g - P_{eq}$, which increases upwards (Figure 4), against the temperature-dependent term, which increases about three-fold downward from the water column to the BHSZ. Hydrate may form or dissociate based on Equation 8, but because the HSZ is always populated with gas for these simulations, $P_g \geq P_{eq}$ in this region and hydrate only forms and never dissociates.

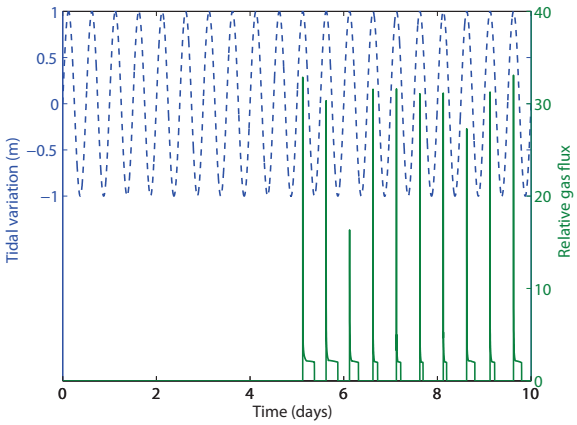

Figure 10: Spatial discretization sensitivity with $nz = 64$ and $dz = 2.8$ m, compared with $nz = 32$ and $dz = 5.6$ m in Figure 3. Increasing the spatial discretization causes the initial peaks in gas release to be larger due to the stronger gas pressure gradient between the top cell and seafloor. In both these cases, the finite volume interface permeabilities were estimated from the cell values using a moving average filter with enough cells to cover a width of 10 m.

Numerical techniques. The flow Equations (4–6) are discretized in space using a finite volume method with first-order upwinding and integrated in time using a forward Euler scheme. The model is sensitive to the spatial discretization because of the nonlinear relationship between permeability and effective stress through conduit dilation. This means that the gas pressure gradients which build up at the top of the sediment column are larger for finer discretization, and hence the driving force for gas flow is stronger and the initial peak in ebullition is larger (compare Figures 3 and 10).

The model timestep is chosen dynamically to keep the magnitude of gas pressure changes from flow and hydrate formation small compared with the sediment strength. This condition is strict enough that the results do not change when a smaller timestep is imposed.

Discussion and Conclusions. The model developed here shows that free gas flow through dynamic conduits is a potential mechanism by which tides trigger ebullition from hydrate-bearing sediments at South Hydrate Ridge [40, 41] (Figure 3). Although the model neglects spatial heterogeneity and processes that control the long-term dynamics of hydrate-bearing sediments, its ability to balance free-gas flow through dynamic conduits against conversion to hydrates allows us to identify emergent behavior and the relevant temporal and spatial scales that may control venting at the seafloor. For example, the tidal forcing imposes gas-flux periodicity on the release of connected gas plumes that rise through the HSZ, and within a tidal ebb the release may break into multiple bursts as the flow conduit opens and closes near the surface, in a mechanism reminiscent of fluid expulsion from a geyser.

This fraction of injected gas that escapes conversion to hydrate is sensitive to the timescales of fluid flow and hyrdate formation. More gas escapes conversion to hydrate when the ratio $t_{hydrate}/t_{flow}$ is larger, but even at a given value of this ratio, faster hydrate formation causes less gas to survive the rise (Figure 8). We suggest the explanation that gas rises more

slowly as the hydrate formation rate increases because hydrate formation reduces the gas pressure and delays conduit opening. As the time for gas to rise increases, a corrected ratio $t_{hydrate}/t_{flow}$ would be smaller, and the lines might coincide better in Figure 8.

A number of neglected mechanisms impact the efficiency of gas transport and hydrate formation assumed by our model. The transport and accumulation of heat and dissolved methane and salt all tend to inhibit gas flow and hydrate formation and dissociation. Gas and hydrate are only stable when surrounded by methane- saturated pore water, and background aqueous flow flushes away concentrated methane, dissolving gas and hydrates. Our model overestimates the efficiencies of both vertical gas transport and mass transfer from gas to hydrate phases. Meanwhile, salt expulsion from pore water and heat generation during hydrate formation reduce hydrate stability, providing negative feedbacks on hydrate generation.

Given that neither gas flow nor hydrate formation in our model depends on the presence of hydrates, the current model is not an ideal tool for speculating on the impact of gas flow on the vertical hydrate distribution. Future models may be made sensitive to hydrates by considering increased tensile strength [22, 45] or pore clogging [10, 28, 32] with hydrate formation, as well as a dependence of the hydrate formation rate on the available hydrate surface area [21]. Such models may test the stability of hydrate distributions suggested by models that capture long-timescale effects [10, 28, 32] in the presence gas flow through fractures.

Nomenclature

D	mean water depth [m]
E	activation energy [J/mol]
$f_{release}$	fraction of flowing gas released [-]
F_g^{source}	deep source of gas [kg/m^2/s]
g	gravitational acceleration [m/s^2]
H	model domain depth [m]
h_{plume}	height of a rising gas plume [m]
k	intrinsic vertical permeability [m^2]
K_0	lateral stress coefficient [-]
$k_{conduit}$	conduit intrinsic permeability [m^2]
K_h	hydrate formation rate [kg/m^3/Pa/s]
k_{rg}	gas relative permeability [-]
m_{CH_4}	molar mass of methane [kg/mol]
M_g	mass of gas per unit bulk volume [kg/m^3]
M_g^0	initial mass of gas [kg/m^3]
ΔM_g	gas accumulation per unit area [kg/m^2]
P_{eq}	gas-hydrate equilibrium pressure [Pa]
P_g	gas pressure [Pa]
P_h	hydrostatic pressure at sea floor [Pa]
P_w	water pressure [Pa]
R	ideal gas constant [J/mol/K]
S_g	gas saturation [-]

S_g^{min}	minimum gas saturation [-]
$S_g^{conduit}$	minimum open-conduit gas saturation [-]
S_h	hydrate saturation [-]
t	time [s]
t_f	simulation length [s]
t_{flow}	flow timescale [s]
$t_{hydrate}$	hydrate formation timescale [s]
t_{tide}	tidal period [s]
Δt	time step [s]
T	temperature [K]
z	depth below sea floor [m]
z_{BHSZ}	depth of hydrate stability zone base [m]
z_{tide}	tidal height [m]

Greek letters

λ	loading efficiency [-]
μ_g	gas viscosity [Pa.s]
μ_w	water viscosity [Pa.s]
ν	Poisson's ratio [-]
ϕ	porosity [-]
ρ_b	bulk density [kg/m^3]
ρ_g	gas density [kg/m^3]
ρ_w	water density [kg/m^3]
σ	stress (positive in compression) [Pa]
σ'	effective stress [Pa]
σ_h	horizontal stress [Pa]
σ_v	vertical stress [Pa]
σ_C	compressive yield strength [Pa]
σ_T	tensile yield strength [Pa]
σ'_{wv}	vertical water-saturated effective stress [Pa]
σ'_{wv}	vertical water-saturated effective stress [Pa]
$\chi^h_{CH_4}$	mass fraction of methane in hydrates

References

[1] C. K. Algar and B. P. Boudreau. Stability of bubbles in a linear elastic medium: Implications for bubble growth in marine sediments. *J. Geophys. Res.*, 115, 2010.

[2] D. Archer. Methane hydrate stability and anthropogenic climate change. *Biogeosci.*, 4 (4):521–544, 2007.

[3] D. Archer, B. Buffett, and V. Brovkin. Ocean methane hydrates as a slow tipping point in the global carbon cycle. *Proc. Natl. Acad. Sci. U.S.A.*, 106:20596–20601, 2008.

[4] Gaurav Bhatnagar, Walter G. Chapman, Gerald R. Dickens, Brandon Dugan, and George J. Hirasaki. Generalization of gas hydrate distribution and saturation in marine sediments by scaling of thermodynamic and transport processes. *Am. J. Sci.*, 307(6): 861–900, 2007.

[5] A W Bishop. The principle of effective stress. *Teknisk Ukeblad*, 39:859–863, 1959.

[6] BP Boudreau, C Algar, BD Johnson, I Croudace, A Reed, Y Furukawa, KM Dorgan, PA Jumars, AS Grader, and BS Gardiner. Bubble growth and rise in soft sediments. *Geology*, 33(6):517–520, 2005.

[7] B Buffett and D Archer. Global inventory of methane clathrate: sensitivity to changes in the deep ocean. *Earth Planet. Sci. Lett.*, 227(3-4):185–199, 2004.

[8] J.-H. Choi, Y. Seol, R. Boswell, and R. Juanes. X-ray computed-tomography imaging of gas migration in water-saturated sediments: from capillary invasion to conduit opening. 38:L17310, doi:10.1029/2011GL048513, 2011.

[9] Hugh Daigle and Brandon Dugan. Effects of multiphase methane supply on hydrate accumulation and fracture generation. *Geophys. Res. Lett.*, 37, 2010.

[10] Hugh Daigle and Brandon Dugan. Origin and evolution of fracture-hosted methane hydrate deposits. *J. Geophys. Res.*, 115, 2010.

[11] G R Dickens, J R O'Neil, D K Rea, and R M Owen. Dissociation of oceanic methane hydrate as a cause of the carbon-isotope excursion at the end of the paleocene. *Paleoceanography*, 10(6):965–971, 1995.

[12] ZH Duan, N Moller, and JH Weare. An equation of state for the CH4-CO2-H2O system: II. Mixtures from 50 to 1000-degrees-C and 0 to 1000 bar. *Geochim. Cosmochim. Acta*, 56(7):2619–2631, 1992.

[13] PB Flemings, XL Liu, and WJ Winters. Critical pressure and multiphase flow in Blake Ridge gas hydrates. *Geology*, 31(12):1057–1060, 2003.

[14] Sabodh K. Garg, John W. Pritchett, Arata Katoh, Kei Baba, and Tetsuya Fujii. A mathematical model for the formation and dissociation of methane hydrates in the marine environment. *J. Geophys. Res.*, 113(B1), 2008.

[15] Xiaobo Gong, Shu Takagi, and Yoichiro Matsumoto. The effect of bubble-induced liquid flow on mass transfer in bubble plumes. *Int. J. Multiphase Flow*, 35(2):155–162, 2009.

[16] J Greinert and B Nutzel. Hydroacoustic experiments to establish a method for the determination of methane bubble fluxes at cold seeps. *Geo-Mar. Lett.*, 24(2):75–85, 2004.

[17] R. Holtzman and R. Juanes. Thermodynamic and hydrodynamic constraints on overpressure caused by hydrate dissociation: a pore-scale model. 38:L14308, doi:10.1029/2011GL047937, 2011.

[18] A. K. Jain and R. Juanes. Preferential Mode of gas invasion in sediments: Grain-scale mechanistic model of coupled multiphase fluid flow and sediment mechanics. *J. Geophys. Res.*, 114(B08101), 2009.

[19] AG Judd, M Hovland, LI Dimitrov, SG Gil, and V Jukes. The geological methane budget at Continental Margins and its influence on climate change. *Geofluids*, 2(2): 109–126, 2002.

[20] JP Kennett, KG Cannariato, IL Hendy, and RJ Behl. Carbon isotopic evidence for methane hydrate instability during quaternary interstadials. *Science*, 288(5463):128–133, 2000.

[21] HC Kim, PR Bishnoi, RA Heidemann, and SSH Rizvi. Kinetics of methane hydrate decomposition. *Chem. Eng. Sci.*, 42(7):1645–1653, 1987.

[22] A. Klar, K. Soga, and M. Y. A. Ng. Coupled deformation-flow analysis for methane hydrate extraction. *Geotechnique*, 60(10):765–776, 2010.

[23] Michael B. Kowalsky and George J. Moridis. Comparison of kinetic and equilibrium reaction models in simulating gas hydrate behavior in porous media. *Energy Conversion and Management*, 48(6):1850–1863, 2007.

[24] Tae-Hyuk Kwon, Gye-Chun Cho, and J. Carlos Santamarina. Gas hydrate dissociation in sediments: Pressure-temperature evolution. *Geochem. Geophys. Geosyst.*, 9, 2008.

[25] Ira Leifer, Bruce P. Luyendyk, Jim Boles, and Jordan F. Clark. Natural marine seepage blowout: Contribution to atmospheric methane. *Glob. Biogeochem. Cycle*, 20(3), 2006.

[26] AM Leitch and WD Baines. Liquid volume flux in a weak bubble plume. *J. Fluid Mech.*, 205:77–98, 1989.

[27] Xiaoli Liu and Peter Flemings. Dynamic response of oceanic hydrates to sea level drop. *Geophys. Res. Lett.*, 36, 2009.

[28] Xiaoli Liu and Peter B. Flemings. Dynamic multiphase flow model of hydrate formation in marine sediments. *J. Geophys. Res.*, 112(B3), 2007.

[29] D. F. McGinnis, J. Greinert, Y. Artemov, S. E. Beaubien, and A. Wuest. Fate of rising methane bubbles in stratified waters: How much methane reaches the atmosphere? *J. Geophys. Res.*, 111(C9), 2006.

[30] AV Milkov and WY Xu. Comment on "Gas hydrate growth, methane transport, and chloride enrichment at the southern summit of Hydrate Ridge, Cascadia margin off Oregon" by Torres et al. [Earth Planet. Sci. Lett. 226 (2004) 225-241]. *Earth Planet. Sci. Lett.*, 239(1-2):162–167, 2005.

[31] M. Muskat. *Physical Principles of Oil Production*. McGraw-Hill Book Co. (New York), 1949.

[32] J Nimblett and C Ruppel. Permeability evolution during the formation of gas hydrates in marine sediments. *J. Geophys. Res.*, 108(B9), 2003.

[33] Matthew T. Reagan and George J. Moridis. Large-scale simulation of methane hydrate dissociation along the West Spitsbergen Margin. *Geophys. Res. Lett.*, 36, 2009.

[34] C Ruppel, GR Dickens, DG Castellini, W Gilhooly, and D Lizarralde. Heat and salt inhibition of gas hydrate formation in the northern Gulf of Mexico. *Geophys. Res. Lett.*, 32(4), 2005.

[35] B. P. Scandella, C. Varadharajan, H. Hemond, C. Ruppel, and R. Juanes. A conduit dilation model of methane venting from lake sediments. 38:L06408, doi:10.1029/2011GL046768, 2011.

[36] Benjamin P. Scandella, Charuleka Varadharajan, Harold F. Hemond, Carolyn Ruppel, and Ruben Juanes. A conduit dilation model of methane venting from lake sediments. *Geophys. Res. Lett.*, 38(L06408), 2011.

[37] G. C. Sills, S. .J. Wheeler, S. D. Thomas, and N. T. Gardner. Behavior of offshore soils containing gas-bubbles. *Geotechnique*, 41(2):227–241, 1991.

[38] K. Terzaghi. *Theoretical Soil Mechanics*. John Wiley, New York, 1943.

[39] Stephen David Thomas. *The consolidation behaviour of gassy soil*. PhD thesis, University of Oxford, 1987.

[40] M. E. Torres. , 2010. Pers. comm.

[41] M.E. Torres, J. McManus, D.E. Hammond, M.A. de Angelis, K.U. Heeschen, S.L. Colbert, M.D. Tryon, K.M. Brown, and E. Suess. Fluid and chemical fluxes in and out of sediments hosting methane hydrate deposits on Hydrate Ridge, OR, I: Hydrological provinces. *Earth Planet. Sci. Lett.*, 201(3-4):525 – 540, 2002.

[42] ME Torres, K Wallmann, AM Trehu, G Bohrmann, WS Borowski, and H Tomaru. Reply to comment on: "Gas hydrate growth, methane transport and chloride enrichment at the southern summit of Hydrate Ridge, Cascadia Margin off Oregon". *Earth Planet. Sci. Lett.*, 239(1-2):168–175, 2005.

[43] AM Trehu, PB Flemings, NL Bangs, J Chevallier, E Gracia, JE Johnson, CS Liu, XL Liu, M Riedel, and ME Torres. Feeding methane vents and gas hydrate deposits at south Hydrate Ridge. *Geophys. Res. Lett.*, 31(23), 2004.

[44] DL Valentine, DC Blanton, WS Reeburgh, and M Kastner. Water column methane oxidation adjacent to an area of active hydrate dissociation, Eel River Basin. *Geochim. Cosmochim. Acta*, 65(16):2633–2640, 2001.

[45] W. F. Waite, J. C. Santamarina, D. D. Cortes, B. Dugan, D. N. Espinoza, J. Germaine, J. Jang, J. W. Jung, T. J. Kneafsey, H. Shin, K. Soga, W. J. Winters, and T-S. Yun. Physical properties of hydrate-bearing sediments. *Reviews of Geophysics*, 47, 2009.

[46] Herbert F. Wang. *Theory of Linear Poroelasticity with Applications to Geomechanics and Hydrogeology*. Princeton University Press, 2000.

[47] JL Weinberger and KM Brown. Fracture networks and hydrate distribution at Hydrate Ridge, Oregon. *Earth Planet. Sci. Lett.*, 245(1-2):123–136, 2006.

[48] WY Xu and C Ruppel. Predicting the occurrence, distribution, and evolution of methane gas hydrate in porous marine sediments. *J. Geophys. Res.*, 104(B3):5081–5095, 1999.

National Energy Technology Laboratory

626 Cochrans Mill Road
P.O. Box 10940
Pittsburgh, PA 15236-0940

3610 Collins Ferry Road
P.O. Box 880
Morgantown, WV 26507-0880

One West Third Street, Suite 1400
Tulsa, OK 74103-3519

1450 Queen Avenue SW
Albany, OR 97321-2198

2175 University Ave. South
Suite 201
Fairbanks, AK 99709

Visit the NETL website at:
www.netl.doe.gov

Customer Service:
1-800-553-7681